Plasmoelectric potentials in metal nanostructures

Matthew T. Sheldon *et al.*

Science **346**, 828 (2014);
DOI: 10.1126/science.1258405

REPORTS

NANOPHOTONICS

Plasmoelectric potentials in metal nanostructures

Matthew T. Sheldon,[1] Jorik van de Groep,[2] Ana M. Brown,[1] Albert Polman,[2] Harry A. Atwater[1]*

The conversion of optical power to an electric potential is of general interest for energy applications and is typically obtained via optical excitation of semiconductor materials. We developed a method for achieving electric potential that uses an all-metal geometry based on the plasmon resonance in metal nanostructures. In arrays of gold nanoparticles on an indium tin oxide substrate and arrays of 100-nanometer-diameter holes in 20-nanometer-thick gold films on a glass substrate, we detected negative and positive surface potentials during monochromatic irradiation at wavelengths below or above the plasmon resonance, respectively. We observed plasmoelectric surface potentials as large as 100 millivolts under illumination of 100 milliwatts per square centimeter. Plasmoelectric devices may enable the development of all-metal optoelectronic devices that can convert light into electrical energy.

Noble metal nanostructures display remarkable optical properties that arise from the coupling of incident light to the collective motion of the conduction electrons. The excitation, propagation, and localization of these plasmons can be tailored by nanoscale control of metal size and shape (*1*). Metal nanostructures exhibiting subwavelength optical confinement (*2*) have enabled nanoscale photonic waveguides, modulators, enhancement of second-harmonic generation, light-trapping structures for photovoltaics, and biological labeling techniques (*1*, *2*). Coupling of laser light to plasmonic structures can also result in efficient localized heating, because the resonant absorption cross section for plasmonic nanostructures is much larger than their physical cross section.

Recent work has demonstrated control over the plasmon resonance frequency (ω_p) of metal nanostructures when an external electrostatic field alters the carrier density in the metal (*3*). Increasing the carrier density in a noble metal nanoparticle leads to a blueshift of the resonance, whereas decreasing it leads to a redshift, as illustrated for a 20-nm-diameter Ag nanoparticle in vacuum (Fig. 1). The reverse effect—the optical generation of an electrostatic potential due to an optically driven change in carrier density in a plasmonic nanostructure—has so far not been observed. Thermodynamically, however, such a plasmoelectric effect is expected to occur. We obtained direct experimental evidence of plasmoelectric potentials in the range 10 to 100 mV on colloidal assemblies and plasmonic light-harvesting device geometries, in qualitative agreement with a thermodynamic model. These results may provide a new route to convert optical energy into electrical power.

Figure 2A shows the measured scattering spectrum for 60-nm Au colloids on indium tin oxide (ITO)/glass, showing a clear plasmon resonance around λ = 550 nm. To probe the local static potential difference between the tip and sample surface at room temperature, we used Kelvin probe force microscopy (KPFM) (*4*) with a conductive atomic force microscope tip in noncontact mode (Fig. 2). While the illumination wavelength was gradually scanned through the plasmon resonance spectrum, from 480 to 650 nm (~1 nm s^{-1}), we probed the potential on the illuminated Au nanoparticle array (*5*). A clear optically induced surface potential was observed, which varied with illumination wavelength (Fig. 2B). We observed negative induced potentials during excitation to the blue side of the neutral-particle plasmon resonance wavelength near 550 nm, and positive potentials during excitation on the red side of the resonance, with the measured potential changing sign near the peak of the plasmon resonance.

To model the experimentally observed plasmoelectric effect, we consider a metal nanostructure placed on a grounded conducting substrate that is illuminated with monochromatic radiation at a wavelength just below the plasmon resonance λ_p. Random charge fluctuations between particle and substrate will cause the plasmon resonance spectrum to vary by minute amounts (Fig. 1). If an electron is randomly added to the particle, the resonance will shift toward the blue, leading to a concomitant increase in light absorption of the particle, which in turn leads to a small increase in the nanoparticle temperature. The changes in number of electrons N and temperature $T(N)$ change the free energy F of the particle, and an equilibrium charge density is achieved when the free energy is at a minimum:

$$\frac{\partial F(N,T)}{\partial N} = \left(\frac{\partial F}{\partial N}\right)_T + \left(\frac{\partial F}{\partial T}\right)_N \frac{dT}{dN} = 0 \quad (1)$$

Here, we assume that both the intensity and wavelength of the illumination are constant. Using, by definition, $(\partial F/\partial N)_T \equiv \mu$, where μ is the electrochemical potential, and $-(\partial F/\partial T)_N \equiv S$, where S is the entropy of the particle, we find

$$\mu = S\frac{dT}{dN} \quad (2)$$

Equation 2 shows that under illumination, the plasmonic particle adopts an electrochemical potential that is proportional to dT/dN. This quantity, which is determined only by the plasmon resonance spectrum and the heat flow from the particle to the substrate, provides the unique thermodynamic driving force in this system. It favors charge transfer to or from the particle that increases absorption, and thereby temperature, in order to lower the free energy. The factor dT/dN is largest on the steepest parts of the resonance spectrum; it is positive for irradiation on the blue side of the resonance, leading to a positive chemical potential for the electrons and hence a negative voltage. The reverse is

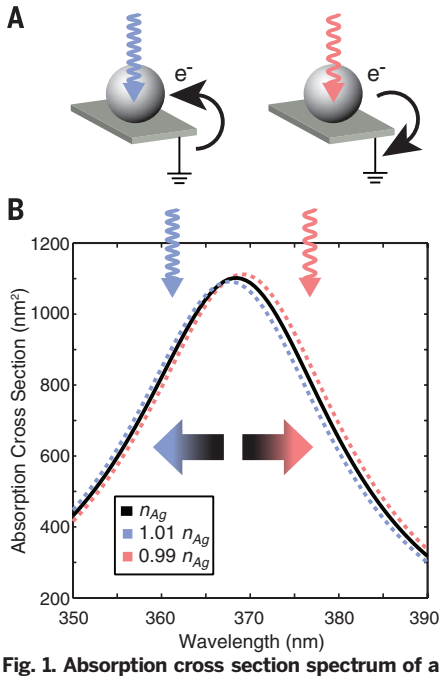

Fig. 1. Absorption cross section spectrum of a Ag nanoparticle and the plasmoelectric effect. (**A**) Schematics: Spontaneous charge transfer to or from the nanoparticle is thermodynamically favored when the consequent spectral shift increases the absorption, raising the temperature. Irradiation on the blue side of the resonance leads to a negative charge on the particle; irradiation on the red side leads to a positive charge. (**B**) Calculated absorption cross section for a 20-nm-diameter Ag nanoparticle in vacuum with bulk carrier density nAg and carrier densities that are reduced or increased by 1%.

[1]Thomas J. Watson Laboratories of Applied Physics, California Institute of Technology, MC 128-95, Pasadena, CA 91125, USA. [2]Center for Nanophotonics, FOM Institute AMOLF, Science Park 104, 1098 XG Amsterdam, Netherlands.
*Corresponding author. E-mail: haa@caltech.edu

observed for irradiation on the red side of the resonance. All these trends are exactly as observed in the experimental spectra of Fig. 2B: The surface potential vanishes at the peak of the resonance where dT/dN is zero; the largest (negative) potential is observed at a wavelength of 500 nm, coinciding with the steepest slope in the resonance spectrum of Fig. 2A.

Equation 1 can be used to quantitatively estimate the equilibrium plasmoelectric potential by writing $F(N, T)$ as the sum of the free energies of electrons and phonons, using the well-known free energy functions of an electron and phonon gas (*6*, *7*). The electronic term is composed of a contribution due to the chemical potential of the electrons that is directly given by the Fermi function, and an electrostatic contribution due to charging of the metal nanosphere; the phonon term is given by the Debye model. Taking the derivatives to N and T, we find analytical expressions for $\mu(N, T)$ and $S(N, T)$ that are then input into Eq. 2 (*5*).

Before applying the model to the experimental geometry in Fig. 2, we first calculated the plasmoelectric potential (i.e., the electrochemical potential gained by the particle from the electron transfer induced by optical absorption) for a spherical 20-nm-diameter Ag nanoparticle in vacuum under monochromatic illumination. For these particles, analytical Mie theory can be used to calculate the absorption cross section spectrum, $C_{abs}(\lambda, n)$, for a given electron density in the nanoparticle by taking into account the dependence of the bulk plasma frequency, ω_p, in the complex dielectric function of the metal on carrier density, $\omega_p \propto n^{1/2}$ (*5*). To calculate the nanoparticle temperature, we used a steady-state heat-flow model in which heat is dissipated from the nanoparticle by radiation. Figure 3A shows the calculated plasmoelectric potential of the Ag nanoparticle as a function of illumination wavelength at an incident flux of 1 mW/cm^2, under which the particle obtains a maximum temperature of ~400 K (*5*). The model predicts a clear negative surface potential below the plasmon resonance and a positive one, up to 150 mV, above it. The asymmetry in the plasmoelectric potential below and above the resonance wavelength is due to the intrinsic nonresonant interband absorption in the metal. Figure 3B shows the corresponding relative absorption increase for the Ag nanoparticle, which ranges up to 2.5×10^{-5}.

The model for the simple geometry in Fig. 3 describes the key factors in the plasmoelectric effect: an increase in carrier density under illumination at wavelengths shorter than the resonance peak, inducing a negative plasmoelectric potential and enhanced absorption relative to the neutral particle. Similarly, radiation at longer wavelengths induces a lower carrier density, a positive plasmoelectric potential, and enhanced absorption. These results demonstrate that an excited plasmonic resonator behaves as a heat engine that can convert absorbed off-resonant optical power into a static electrochemical potential.

Next, we used the model to calculate the wavelength-dependent and power-dependent plasmoelectric potential for the experimental geometry in Fig. 2, a spherical 60-nm-diameter Au particle on an ITO/glass substrate. We calculated the factor dT/dN in Eq. 2 using finite-difference time domain (FDTD) simulations of the absorption spectra for an Au particle on an ITO/glass substrate to take into account radiative damping from the substrate not captured by simple Mie theory and a one-dimensional model for heat conduction into the substrate (*5*). Because of variations in interparticle coupling and clustering [see scanning electron microscopy (SEM) image in Fig. 2A] and possible adsorption of water onto the particle-ITO interface, the ensemble dielectric environment is complex. The broadened, redshifted scattering spectrum in Fig. 2A is evidence for some particle aggregation. In the FDTD simulations, we modeled these effects by assuming a background index of $n = 1.4$ for the medium above the ITO substrate, such that the absorption spectrum matched the experimentally observed spectrum. As can be seen in Fig. 2C for the high-power data, the modeled trends correspond well with the experimental trends: The modeled minimum potential occurs at 530 nm (experimental: 500 nm), the modeled zero potential

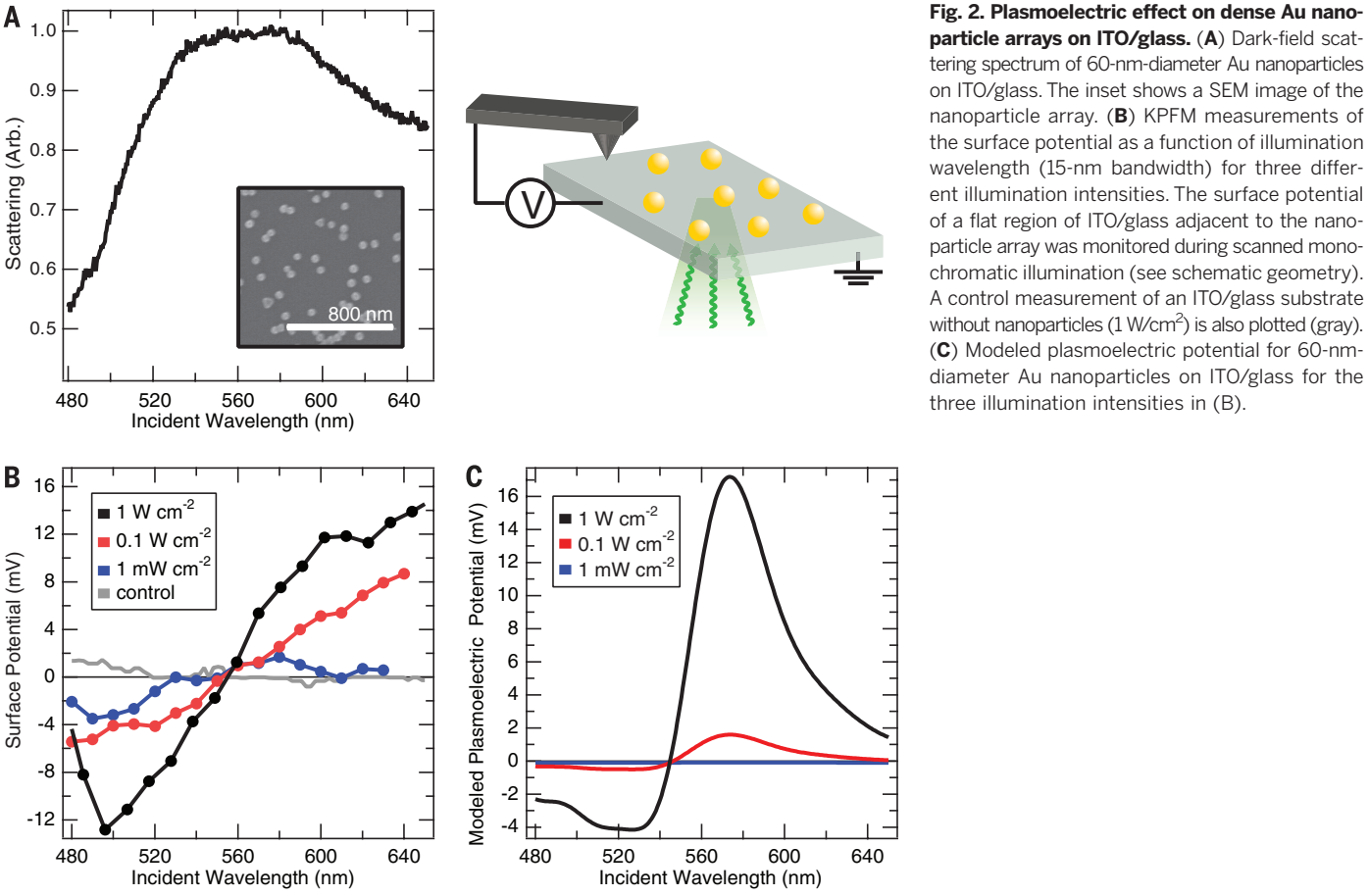

Fig. 2. Plasmoelectric effect on dense Au nanoparticle arrays on ITO/glass. (**A**) Dark-field scattering spectrum of 60-nm-diameter Au nanoparticles on ITO/glass. The inset shows a SEM image of the nanoparticle array. (**B**) KPFM measurements of the surface potential as a function of illumination wavelength (15-nm bandwidth) for three different illumination intensities. The surface potential of a flat region of ITO/glass adjacent to the nanoparticle array was monitored during scanned monochromatic illumination (see schematic geometry). A control measurement of an ITO/glass substrate without nanoparticles (1 W/cm^2) is also plotted (gray). (**C**) Modeled plasmoelectric potential for 60-nm-diameter Au nanoparticles on ITO/glass for the three illumination intensities in (B).

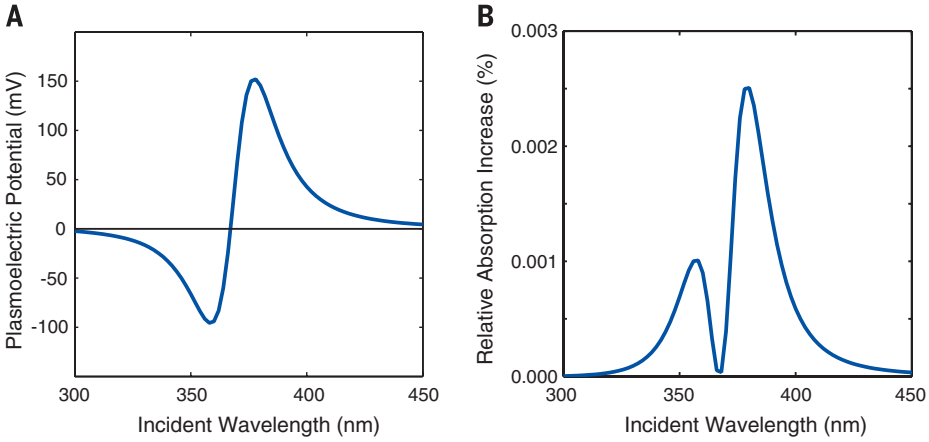

Fig. 3. Modeled plasmoelectric response for Ag nanoparticles. A 20-nm-diameter Ag particle in vacuum is illuminated with monochromatic light (1 mW/cm^2). (**A**) Plasmoelectric potential and (**B**) relative absorption increase as a function of incident wavelength.

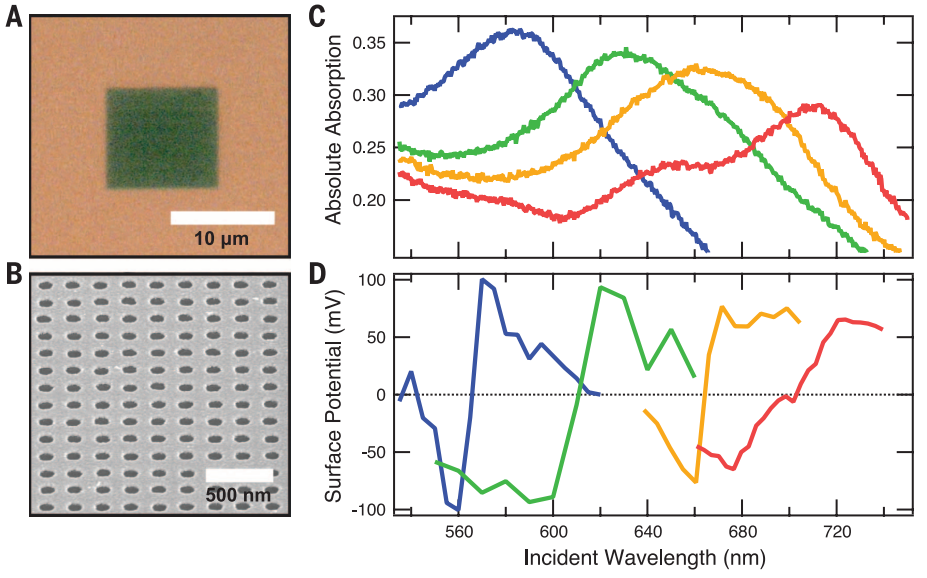

Fig. 4. Plasmoelectric effect on Au nanohole arrays on glass. (**A**) Bright-field optical microscope image showing a 200-nm-pitch array of 100-nm-diameter holes in a 20-nm-thick Au film on glass. The dark green color directly shows the strong absorption in the hole array. (**B**) SEM image of a 200-nm-pitch hole array imaged under 52° with respect to the normal. (**C**) Measured optical absorption spectra for hole arrays with a pitch of 175 nm (blue), 225 nm (green), 250 nm (yellow), and 300 nm (red) (NA = 0.8). (**D**) Surface potential as a function of excitation wavelength measured using KPFM at 100 mW/cm^2 for the four-hole arrays in (C) (NA = 0.25).

occurs at 545 nm (experimental: 560 nm), and a large positive potential is observed for wavelengths above the resonance, both in model and experiment. The extent of the measured potential to wavelengths up to 640 nm in Fig. 2B is in agreement with the long-wavelength tail in the spectrum of Fig. 2A. At 555 nm, the modeled particle temperature peaks at 308 K, 15 K above ambient (*5*), in good agreement with other experimental observations (*8*).

To aid interpretation of our findings, we comment briefly on other mechanisms for generating photopotentials with metals. A thermoelectric effect is several orders of magnitude weaker (~μV K^{-1}) than the observed potentials (*9*). Hot carrier–induced effects would require rectifying contacts, which are not present in our geometry. Moreover, both of these effects would not result in a bisignated signal (*10*). "Plasmon drag" or similar direct photon-to-electron momentum transfer mechanisms on Au colloids would not produce a bisignated signal, nor would the hole arrays described below under normal-incidence irradiation (*11*). Future work in this area will benefit from further insight into the microscopic mechanisms that contribute to the observed effect.

To demonstrate the generality of the observed plasmoelectric effect, we measured the plasmoelectric potential on arrays of subwavelength holes in an optically thin Au film on a glass substrate. In these microarrays, light is absorbed by the resonant excitation of interacting surface plasmon polaritons that propagate between the holes on the Au-air and Au-glass interface (*5*, *12*). The absorption spectrum of a single array is determined by the coherent interaction of plasmons within the array, and the study of such arrays thus enables probing the plasmoelectric effect on a single absorber geometry. Moreover, the metal hole array architectures provide a first step toward future plasmoelectric integrated circuitry in which plasmoelectric power is harvested.

Figure 4, A and B, shows a fabricated 10 μm by 10 μm hole array composed of 100-nm-diameter holes in a square array with a pitch of 200 nm, made in a 20-nm-thick Au film on a glass substrate. Figure 4C shows the measured absorption spectra of hole arrays with a pitch of 175 to 300 nm (*5*). Increasing the pitch leads to a clear redshift in the absorption spectrum. Figure 4D shows the corresponding measured surface potential as a function of the wavelength of illumination (100 mW cm^{-2}), as measured with KPFM. A transition from negative to positive surface potential is seen for each array geometry. Also, the measured potential spectra show a clear redshift with increasing array pitch, in accordance with the trend in the absorption spectra. The maximum plasmoelectric potential observed for each measurement shows a gradually decreasing trend with increasing pitch, also in agreement with the trend in the absorption spectra. A slight difference is observed between the zero-crossing in the potential measurements and the peak in the corresponding absorption spectrum, which is attributed to the difference in numerical aperture (NA) of the microscope objective used for the two measurements (*5*). All surface potential spectra show clear minima and maxima and then decrease as the wavelength is tuned further away from the resonance, as expected. The measurements in Fig. 4D show a plasmoelectric potential as large as ±100 mV and demonstrate the generality of the plasmoelectric effect for arbitrary plasmonic absorbers.

The observed plasmoelectric phenomenon takes advantage of the remarkable spectral tailorability of plasmonic nanostructures and can be extended to a variety of material systems, absorber geometries, and radiation environments. Plasmoelectric devices may enable the development of entirely new types of all-metal optoelectronic devices that can convert light into electrical energy by replacing the usual function of doped semiconductors with metal nanostructures that are optically excited off-resonance.

REFERENCES AND NOTES

1. J. A. Schuller *et al.*, *Nat. Mater.* **9**, 193–204 (2010).
2. L. Novotny, N. van Hulst, *Nat. Photonics* **5**, 83–90 (2011).

3. C. Novo, A. M. Funston, A. K. Gooding, P. Mulvaney, *J. Am. Chem. Soc.* **131**, 14664–14666 (2009).
4. M. Nonnenmacher, M. P. O'Boyle, H. K. Wickramasinghe, *Appl. Phys. Lett.* **58**, 2921 (1991).
5. See supplementary materials on *Science* Online.
6. N. W. Ashcroft, N. D. Mermin, *Solid State Physics* (Harcourt, New York, 1976).
7. B. M. Askerov, S. Figarova, *Thermodynamics, Gibbs Method and Statistical Physics of Electron Gases* (Springer, New York, 2010).
8. M. G. Cerruti *et al.*, *Anal. Chem.* **78**, 3282–3288 (2006).
9. F. J. Blatt, P. A. Schroeder, C. F. Foiles, *Thermoelectric Power of Metals* (Plenum, New York, 1976).
10. M. W. Knight, H. Sobhani, P. Nordlander, N. J. Halas, *Science* **332**, 702–704 (2011).
11. N. Noginova, A. V. Yakim, J. Soimo, L. Gu, M. A. Noginov, *Phys. Rev. B* **84**, 035447 (2011).
12. W. L. Barnes, W. A. Murray, J. Dintinger, E. Devaux, T. W. Ebbesen, *Phys. Rev. Lett.* **92**, 107401 (2004).

ACKNOWLEDGMENTS

Supported by U.S. Department of Energy (DOE) Office of Science grant DE-FG02-07ER46405 (M.S. and H.A.A.), an NSF Graduate Research Fellowship (A.B.), and experimental facilities of the DOE "Light-Material Interactions in Energy Conversion" Energy Frontier Research Center grant DE-SC0001293. Work at AMOLF is part of the research program of the Foundation for Fundamental Research on Matter [which is financially supported by the Netherlands Organization for Scientific Research (NWO)] and by the European Research Council. The data are archived in the laboratory of H.A.A. and A.P. We thank E. Kosten, V. Brar, D. Callahan, M. Deceglie, A. Leenheer, J. Fakonas, R. van Roij, B. M. Mulder, and H. J. Bakker for helpful discussions.

SUPPLEMENTARY MATERIALS

www.sciencemag.org/content/346/6211/828/suppl/DC1
Materials and Methods
Supplementary Text
Figs. S1 to S9
References (*13*–*36*)

7 July 2014; accepted 16 October 2014
Published online 30 October 2014;
10.1126/science.1258405

INTERFACIAL WATER

The structure of interfacial water on gold electrodes studied by x-ray absorption spectroscopy

Juan-Jesus Velasco-Velez,[1] Cheng Hao Wu,[1,2] Tod A. Pascal,[3] Liwen F. Wan,[3] Jinghua Guo,[4,5] David Prendergast,[3] Miquel Salmeron[1,6]*

The molecular structure of the electrical double layer determines the chemistry in all electrochemical processes. Using x-ray absorption spectroscopy (XAS), we probed the structure of water near gold electrodes and its bias dependence. Electron yield XAS detected at the gold electrode revealed that the interfacial water molecules have a different structure from those in the bulk. First principles calculations revealed that ~50% of the molecules lie flat on the surface with saturated hydrogen bonds and another substantial fraction with broken hydrogen bonds that do not contribute to the XAS spectrum because their core-excited states are delocalized by coupling with the gold substrate. At negative bias, the population of flat-lying molecules with broken hydrogen bonds increases, producing a spectrum similar to that of bulk water.

Many important processes in electrochemical reactions, such as ion desolvation and charge transfer, occur in the so-called electrical double layer (EDL), also known as the Helmholtz layer (*1*). This layer, containing solvated ions and solvent molecules, is typically one to tens of nanometers thick, depending on solute concentration. An important characteristic of the EDL is the presence of a strong electric field perpendicular to the electrode surface that is believed to play a crucial role in determining its structure.

Among liquids, aqueous solutions play a vital role in chemistry, biology, and materials sciences. The strong dipole of the water molecule and its hydrogen-bonding network gives rise to distinctive properties, including the high boiling point and high specific heat capacity. It is expected therefore that perturbations of the local hydrogen bonding network near surfaces (*2*, *3*), together with strong electric fields, will influence the structure of the first molecular layers. Understanding the structure and dynamics of these interface layers is of fundamental importance and the object of our study.

A host of techniques have been used to study the EDL, including grazing incidence x-ray scattering (*4*) that provides crystallographic information and electronic density profiles, and vibration spectroscopies such as infrared (IR) and Raman (*5*, *6*), together with nonlinear second-order sum frequency generation (SFG), which have been used to study the vibrational nature of water molecules at interfaces (*7*). Using SFG at the glass-water interface at different pH values, it was concluded that protonation and deprotonation of oxide sites led to surface charges and electric fields that align the interfacial water molecules (*8*–*10*).

In contrast to these techniques, x-ray absorption spectroscopy (XAS) is element-specific and provides information about the electronic structure around the excited atom, which is sensitive to the local structure and chemical environment (*11*). XAS has been extensively used to study the structure of water by analyzing the oxygen K-edge spectra (*12*, *13*). XAS can be performed by collecting either photons or secondary electrons generated by the decay of the core holes created by the absorbed x-rays. The first detection mode, called total fluorescence yield (TFY) (*14*–*17*), is a bulk-sensitive technique, because the mean free path of soft x-rays is in the micrometer range. When collecting secondary electrons (the so-called total electron yield mode, TEY), the information is surface sensitive because of the short mean free path of electrons in condensed matter, on the order of nanometers for energies in the 100-eV range.

Our system consists of an electrochemical flow cell with an ultrathin Si_3N_4 membrane window (100 nm thick) that separates the liquid medium inside the cell from the high-vacuum environment of Beamline 8.0.1 in the Advanced Light Source at the Lawrence Berkeley National Laboratory (Fig. 1). The cell contains reference and counter electrodes for electrochemical experiments (*18*, *19*). The electrode under study is a ~20-nm Au film evaporated on the internal side of the Si_3N_4 membrane, in contact with a flowing aqueous 10 μM solution of NaCl. The film is continuous and fully covers the membrane surface, as shown by atomic force microscopy (AFM) imaging (fig. S1) (*20*). Gold was chosen because its inert nature makes it possible to explore a wide range of electrostatic potentials without inducing electrolysis or other electrochemical reactions that could alter the structure and composition of its surface. The lack of reactivity or ion adsorption was confirmed by the absence of peaks in the cyclic voltammetry curves (fig. S2) (*20*). Because the effective attenuation length of electrons with energy smaller than 530 eV (from the O K-edge excitation of water) is estimated to be between 5 and 10 Å in liquid water (*21*, *22*), the TEY signal should originate from the first two or three water layers. This was confirmed by theoretical calculations as discussed below.

Figure 2A shows the O K-edge XAS spectra of water at open circuit potential in TFY (curve a), and TEY detection modes (curves b and c). Curve a corresponds to the well-known oxygen K-edge spectrum of bulk water, which is divided into three regions: pre-edge region, around 535 eV (I); main edge region, around 537 eV (II); and post-edge region, around 540 eV (III). The pre-edge peak at 535 eV is characteristic of the liquid phase

[1]Materials Science Division, Lawrence Berkeley National Laboratory, Berkeley, CA 94720, USA. [2]Department of Chemistry, University of California, Berkeley, CA 94720, USA. [3]Joint Center for Energy Storage Research, The Molecular Foundry, Lawrence Berkeley National Laboratory, Berkeley, CA 94720, USA. [4]The Advanced Light Source, Lawrence Berkeley National Laboratory, Berkeley, CA 94720, USA. [5]Department of Chemistry and Biochemistry, University of California, Santa Cruz, CA 95064, USA. [6]Department of Materials Science and Engineering, University of California, Berkeley, CA 94720, USA.
***Corresponding author. E-mail: mbsalmeron@lbl.gov**